Research Article

4D Printing of Triple-Shape Memory Cyanate Composites Based on Interpenetrating Polymer Network Structures

Linlin Wang, Fenghua Zhang, Shanyi Du, and Jinsong Leng*

Cite This: *ACS Appl. Mater. Interfaces* 2023, 15, 21496−21506

Read Online

ACCESS | Metrics & More | Article Recommendations | Supporting Information

ABSTRACT: The triple-shape memory polymer (TSMP) can be programmed into two temporary shapes (S_1 and S_2) and shows an ordinal recovery from S_2 to S_1 and eventually to the permanent shape upon heating, which realizes more complex stimulus-response motions. We introduced a novel strategy for forming triple-shape memory cyanate ester (TSMCE) resins with high strength and fracture toughness via three-step curing, including four-dimensional (4D) printing, UV post-curing, and thermal curing. The obtained TSMCE resins presented two separated glass transition temperature (T_g) regions due to the formation of an interpenetrating polymer network (IPN), which successfully endowed the polymers with the triple-shape memory effect. The two T_g increased with the increasing cyanate ester (CE) prepolymer content; their ranges were 82.7−102.1 °C and 164.4−229.0 °C, respectively. The fracture strain of the IPN CE resin was up to 10.9%. Moreover, the cooperation of short carbon fibers (CFs) and glass fibers (GFs) with the polymer-accelerated phase separation resulted in two well-separated T_g peaks exhibiting better excellent triple-shape memory behaviors and fracture toughness. The strategy for combining the IPN structure and 4D printing provides insight into the preparation of shape memory polymers integrating high strength and toughness, multiple-shape memory effect, and multifunctionality.

KEYWORDS: *shape memory cyanate, composites, interpenetrating polymer network, triple-shape memory effect, 4D printing*
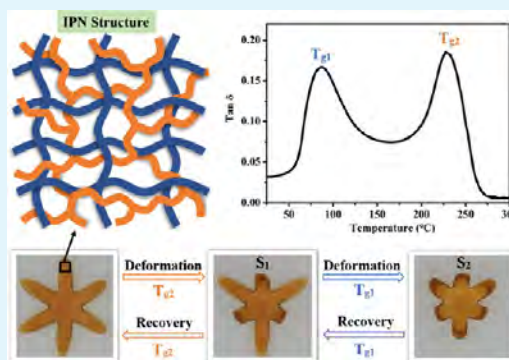
1. INTRODUCTION

A typical shape memory polymer (SMP) is deformed to a temporary shape and recovers to its permanent shape under the external physical or chemical stimuli, named the dual-shape memory polymer. The typical SMP can only be deformed once, which cannot meet the application demand of multifunctional structures or multistage deployable structures; the research of multiple-SMP has been put on the agenda, among which the research of TSMP has attracted the most attention. TSMP can be programmed into two temporary shapes and recovers sequentially from one temporary shape to the other and eventually to the permanent shape upon heating.[1−6] Compared to the dual-shape memory polymer, TSMP can achieve complex and diverse deformation, which can meet higher requirements and realize multifunctional applications in aerospace, medical devices, sensing, automotive manufacturing, and other fields.

At present, there are four main methods to prepare TSMP. The first is to blend two resins to make the polymer with a wide glass transition region.[7,8] Three-phase blending can also achieve a triple-shape memory effect.[9,10] Another way to obtain TSMP is copolymerization after blending resins to form heterogeneous cross-linking structures and broad glass transition regions.[11−13] The third one is the formation of dynamic covalent bonds in the resin, using the bond fracture

and formation to achieve a triple-shape memory effect.[14−18] The last is to achieve a triple or quadruple SME through the structural design of multiple materials, such as bilayers, laminates, and segmented structures.[19−23] For amorphous SMP, two well-separated glass transition peaks are necessary for the polymers to have outstanding triple-shape memory behaviors. The TSMP prepared by the above methods has a broad glass transition region, and the two glass transition peaks do not separate or overlap in a large area.

Shape memory cyanate ester (SMCE) resins are widely used in the aerospace field because of their excellent mechanical properties and space irradiation resistance. Due to the large amount of triazine rings in the resin, the brittleness and poor deformation ability of the resins greatly limit the application of SMCE in engineering structures; therefore, it is necessary to study their toughening modification. The toughness of pristine cyanate ester (CE) resin is poor, and the fracture strain of modified CE resins at room temperature is difficult to reach

more than 10%, especially for thermoset-modified CE resins.[24−31] It is found that IPN can enhance the mechanical properties of materials,[32−35] and constructing interpenetrating networks in materials may be an excellent way to toughen CE resins. In addition, the preparation of cyanate-based complex structures depends on three-dimensional (3D) printing technology; the second challenge is the successful printing of CE resins. There is little research on the 3D printing of CE resin and its composites. Chandrasekaran et al.[36] prepared a thixotropic ink mixed with silica and CE280, and the ink was processed by direct ink writing. The printed parts were post-cured at 220 and 250 °C, whose fracture strain is 5.2−6.5% and storage modulus is 1.7−1.8 GPa at room temperature. Zhou et al.[37] processed the printable ink by the printer with a UV light source, and the printed gears were thermally cured, resulting in the formation of IPN. The fracture strain of the resin is 1.1−1.6%, and the storage modulus of that is 2.8−3.7 GPa. Tang et al.[24] used a similar method to obtain CE resins with IPN, and their fracture strain is only 4.5−5.6% and storage modulus is 1.9−2.7 GPa. The fracture toughness of printed CE resins is poor and the strength of that is low in the above-published works. To overcome the above problems, poor toughness and low strength of printed CE resins, a novel strategy is introduced for the collaboration between digital light processing (DLP) printing and the IPN structure to prepare triple-shape memory CE resins and their composites, which exhibit two well-separated glass transition regions.

We constructed an IPN structure in a cyanate-based polymer via three-step curing to obtain triple-shape memory CE resins. A blend of photopatternable epoxy acrylate and thermocurable cyanate prepolymer was used as the ink for the DLP printer. The light-induced network initially formed during DLP printing. The printed structures were processed by UV light post-curing to construct the network further, and then the printed objects were thermocured to form another network. The two networks were interpenetrating to form the IPN, which exhibited two well-separated glass transition peaks due to their different thermomechanical behaviors. The fiber-forced CE composites were also printed successfully, and the cooperation of CFs and GFs significantly facilitated phase separation and improved the triple-shape memory performances.

2. EXPERIMENTAL SECTION

2.1. Materials and Methods. 2,2′-Bis(4-cyanatophenyl)propane (CE monomer) was obtained from Jiangsu Wuqiao Resin Factory, China. 2,4,6-Trimethylbenzoyldiphenyl phosphine oxide (TPO) and polyethylene glycol diacrylate (PEGDMA) were purchased from Aladdin. Carbon fibers were purchased from Times Nano, Chengdu Organic Chemicals Co. Ltd. Short glass fibers were obtained from Wuxi Desheng Glass Fiber Technology Co. Ltd, China.

2.2. Preparation of the CE Prepolymer and Printable Inks for Four-Dimensional (4D) Printing. The CE monomer was heated to 120 °C and stirred for 192 h to obtain the CE prepolymer. In our previous work, the epoxy-based oligomer has synthesized via an esterification addition of epoxy and acrylic acid.[38] The yield of the epoxy-based oligomer in the reaction is 68.2%. Most of the unreacted acrylic acid evaporates during the reaction. The epoxy-based oligomer is a mixture of epoxy acrylate and unreacted epoxy. The printable inks were mixtures of the photosensitive epoxy oligomer, PEGDMA, and the CE prepolymer, named CE30, CE40, and CE50, respectively. The component content is listed in Table 1. The PEGDMA could dilute the viscosity of the CE prepolymer to obtain a solvent-free DLP printable ink.

Table 1. Formulations of the Printable Inks

specimens	component content (wt %)			
	CE prepolymer	epoxy-based oligomer	PEGDMA	TPO
CE30	30	30	37	3
CE40	40	20	37	3
CE50	50	10	37	3

2.3. 4D Printing and Post-Curing. The exposure time of a layer was set to 2, 3, and 4 s for CE30, CE40, and CE50, respectively. The time was 4, 5, and 6 s for CE30-CF/GF, CE30-CF/GF, and CE30-CF/GF. 405 nm UV post-curing times were set to 1, 3, 5, 10, 20, 40, and 60 min. The post-cured specimens were labeled P-CE30, P-CE40, and P-CE50. The thermal curing temperature was 150 and 180 °C for 3 h, respectively. The post-cured and heat-cured specimens were named CE30, CE40, and CE50.

2.4. Gel Weight Fraction. The printed rectangular specimens, whose size is 10 mm × 5 mm × 1 mm, were weighed, and their data were recorded as m_1. The weighed specimens were immersed in acetone for 72 h and taken out to dry at 80 °C. The oven-dried specimens were weighed again, and the weights were recorded as m_2. The gel weight fraction (F_w) is calculated by the equation below:

$$F_w = \frac{m_2}{m_1} \times 100\%$$

2.5. Characterizations. The viscosity was measured using a discovery hybrid rheometer (TA Corp.) with a 25 mm parallel plate clamp and a 1000 μm working gap at 25 °C. The surface and fracture surface morphologies of the specimens were exposed by a scanning electron microscope (SEM) (JSM-7600F, JEOL Ltd.) and an optical microscope (Keyence VHX-900, Japan). The samples were sputtered with gold for 30 s before SEM observation. Dynamic mechanical analysis (DMA) of the resins was carried out using a Q800 apparatus (TA Corp.) with a 1 Hz frequency. The size of printed DMA specimens was 30 mm × 3 mm × 1 mm. The stress−strain behavior was performed using a universal testing machine, an Instron 5500 R Universal Testing Machine (Instron Corp.), at a 2 mm/min stretching rate at room temperature. Three samples for each polymer were tested to obtain an average value. The DLP printer printed dumbbell-shaped specimens for the mechanical tensile test. Thermogravimetry analysis (TGA) of the samples was carried out using an analyzer (Mettler-Toledo, Switzerland) from 25 to 800 °C with a 10 °C/min ramp rate.

3. RESULTS AND DISCUSSION

The first step in preparing printable inks is the slow polymerization of the solid CE monomer into a liquid cyanate prepolymer. The CE monomer is white and granular, as shown in Figure S1. The inset of Figure 1a shows photographs of CE prepolymers heated at 120 °C for different times and cooled to room temperature. The prepolymer becomes a flowing liquid after heating for 192 h. The initial viscosity of the prepolymer heated for 192 h is 376.2 Pa·s, and it stabilizes at 253.1 Pa·s after shear thinning.

The viscosity curves of the prepared CE30, CE40, and CE50 inks are shown in Figure 1b, whose initial viscosities are 4.8, 8.5, and 16.1 Pa·s, respectively. The ink viscosity decreases with the increase of shear rate when the shear rate ranges from 0.1/s to 20/s. The viscosity basically remains unchanged when the shear rate increases from 20/s to 120/s. The F_w curves of printed rectangular samples with different post-curing times are plotted in Figure 1c. The changes in F_w are divided into three stages: rapid growth, slow growth, and platform stages. The post-curing time of the printed samples is set to 60 min to ensure adequate cross-linking of the acrylate components. A cubic structure was printed, and its printability has been
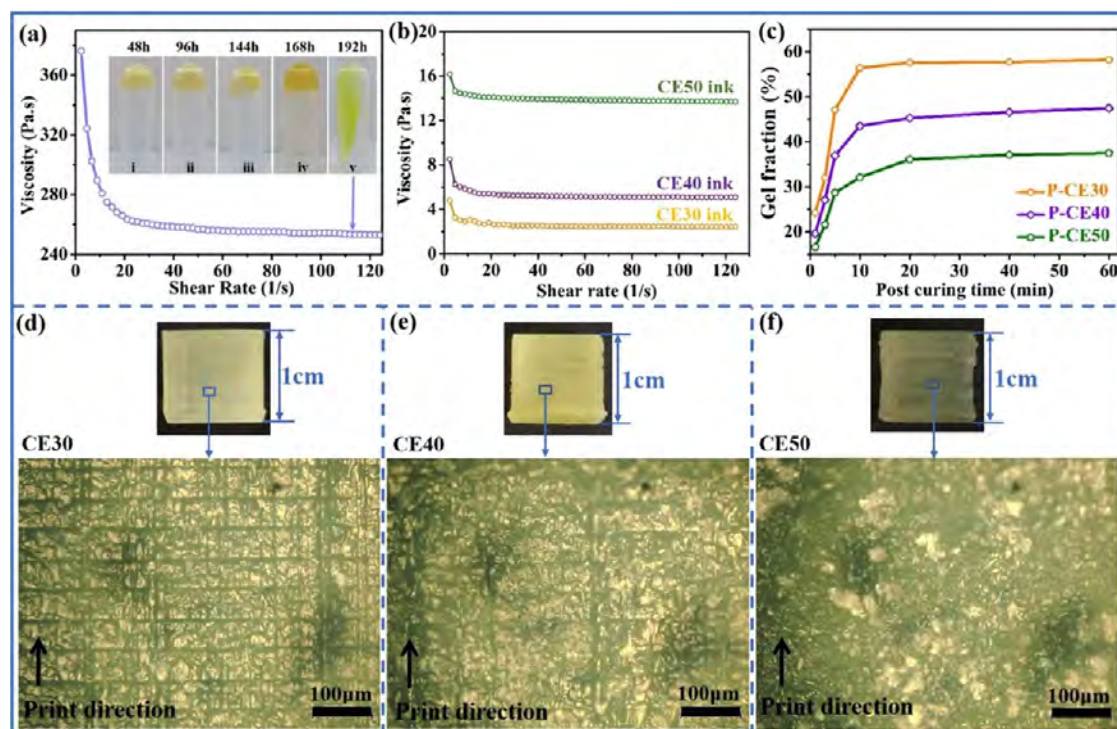
Figure 1. (a) Viscosity curve of the CE prepolymer; (b) viscosity-shear rate curves of CE30, CE40, and CE50 inks; (c) F_w curves of phot-cured resins; and (d−f) optical micrographs of the surfaces of printed CE30, CE40, and CE50 cubes.

validated by CE30, CE40, and CE50 inks. The printed cubes show different morphologies, their accuracy reduces, and the layer structure becomes blurred with the increase of CE content, as shown in Figure 1d−f.

A flower with six petals was printed, and the printed flower was UV post-cured and heat-treated; it varied in color from pale yellow to yellow to brown, as shown in Figure 2a. The IPN structure was gradually formed in the curing process. The epoxy acrylate and PEGDMA reacted, forming a light-induced network (L-network) during DLP printing and UV post-curing, as shown in Figures 2b and S2a. PEGDMA has two roles, the thinner of the printable inks and the modifier of epoxy acrylate, which reacts with epoxy acrylate to form a network structure that acts as a soft segment. During heat treatment, the CE prepolymer self-polymerized, forming triazine rings that acted as cross-linking points in the heat-induced network (H-network). In addition, the unreacted epoxy reacted with the cyano groups in the CE prepolymer, forming a five-membered heterocyclic ring, as shown in Figure S2b. The L-network and H-network are interpenetrated to form IPN in the resin.

The formation of IPN affects the thermodynamic properties of the CE resins. The resin is irradiated by UV lights without heat treatment forming an L-network. The DMA curves of the P-CE40 resin are shown in Figure S3, whose T_g is 56.2 °C. The dynamic mechanical properties of IPN resins with different amounts of CE prepolymer are shown in Figure 2c−e. Two peaks on the tan δ curves demonstrate that the resins have two T_g (T_{g1} and T_{g2}). The T_{g1} is contributed to the L-network and the T_{g2} to the H-network. T_{g1} rose from 94.1 to 102.1 °C and T_{g2} from 164.4 to 221.0 °C. The distance between the two peaks increases with the increased CE prepolymer content. To study the relationship between T_g and CE prepolymer content, the thermodynamic properties of two specimens with 0 and

60% CE prepolymer were tested, and the results are shown in Figure S4a,b. The relationship between T_g and CE prepolymer content is clear, as shown in Figure S4c. The T_{g2} increases gradually with the increase of CE prepolymer content, which is caused by the increasing F_w of the H-network. As the CE prepolymer content increases, the T_{g1} increases first and then decreases. The constraint effect of the H-network on the L-network is the main factor of the increasing T_{g1}, resulting in the poor activity of chains of the L-network and the high temperature required for activation of the chains. When the CE prepolymer content is 60%, the formation of the L-network is restricted. And the F_w of the L-network is greatly reduced, resulting in the decrease of T_{g1}.

The storage modulus increases from 3.0 to 3.5 GPa when the CE prepolymer content is increased to 50%. The tensile test results confirm that the resins, especially the CE30 resin, have good fracture toughness, as shown in Figure 2f. The fracture strain reduces from 10.9% to 7.4% with the increased CE prepolymer content. In addition, the thermal decomposition of the CE30, CE40, and CE50 resins in Figure S5 shows that their initial decomposition temperatures ($T_{5\%}$) are higher than 315 °C. The $T_{5\%}$ of CE50 is up to 338.0 °C, indicating that the resin has good thermal stability and potential applications in devices at high operating temperatures.

The petals of the printed CE40 flower were numbered, as exhibited in Figure 3a. The 1, 3, and 5 petals were reshaped at T_{g2} (181.1 °C) from blooming to closing and then cooled to room temperature. The 2, 4, and 6 petals were reshaped at T_{g1} (98.5 °C). Both programmed shapes could recover to the former shape separately with heating. The shape recovery of the petals proceeded at T_{g1} first and T_{g2} then. There is no sharp line between the shape recovery of 2, 4, and 6 petals and that of 1, 3, and 5 petals because there is some overlap between
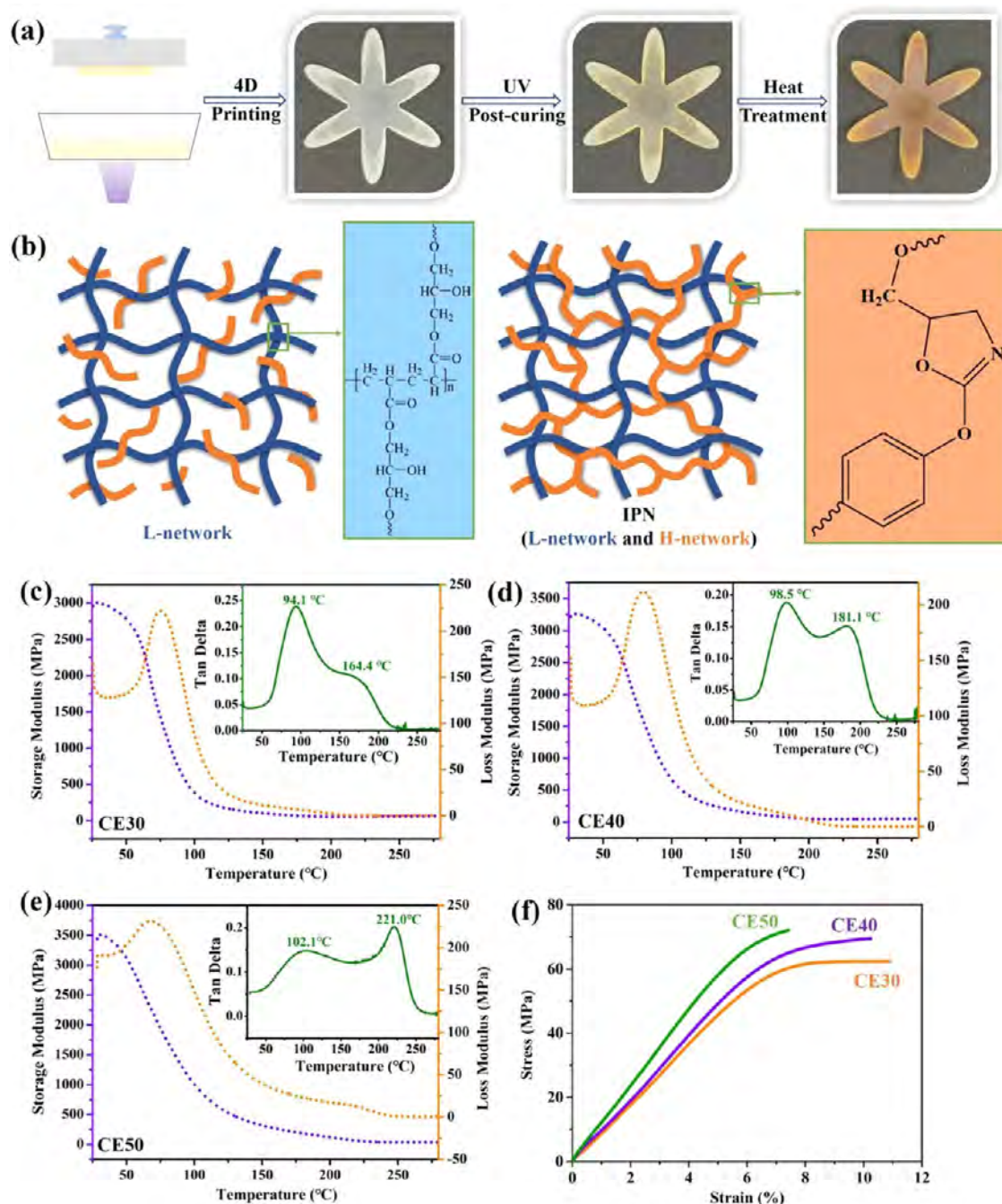
Figure 2. (a) 4D-printed flower of post-curing and heat treatment; (b) networks formed in the specimens; (c−e) DMA curves of printed rectangular specimens; and (f) stress−strain curves of printed dumbbell specimens at room temperature.

the two glass transition peaks. It means that 1, 3, and 5 petals have some recovery when 2, 4, and 6 petals are recovering at T_{g1}. The shape fixity and recovery ratios were calculated by the DMA result, as shown in Figure 3c. The specimen was stretched two times at 190 °C and 100 °C (about 10 °C above T_{g2} and T_{g1}), and the maximal strain was 5.1 and 6.2%, respectively. The shape was fixed, and the strain was 5.4% when the temperature was cooled to 25 °C. The shape fixity ratio was calculated at 87.1%. The specimen was heated to 100 °C and then to 190 °C, which was cooled to 25 °C again. The strain is 0.5%, and the recovery ratio is calculated at 92.0%.

The shape memory behavior of the TSMCE resin is mainly caused by the state and movement of molecular chains in the H-network and L-network. The networks have their own fixed and reversible phases. In the process of shape memory, the state changes of the networks with temperature are shown in Figure S6. When the resin is heated to T_{g2}, the two networks are activated and become a highly elastic state, and the molecular chains have certain mobility. When the temperature is T_{g1}, the L-network is in a highly elastic state, the H-network is in a glassy state, and the mobility of molecular chains is limited. When the molecular chains are stretched in the high elastic state, the elastic potential energy is stored after cooling to room temperature. When it is heated again, the stored potential energy is released, and the shape is restored.
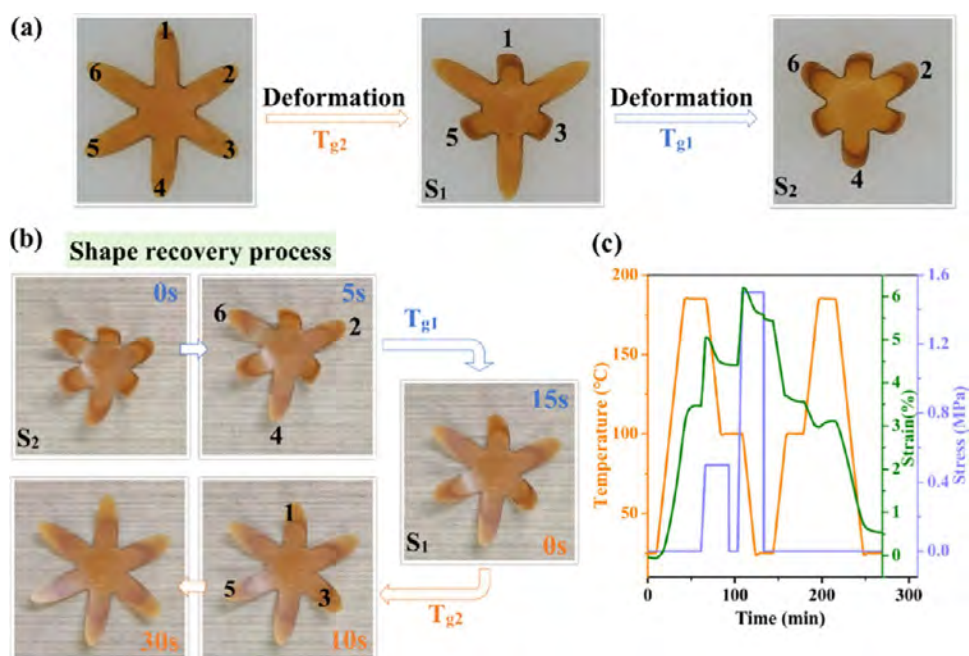
Figure 3. Triple-shape memory behaviors of the 4D-printed flower: (a) Deformation of temporary shapes (S_1 and S_2); (b) triple-shape recovery process of the printed flower; and (c) triple-shape fixity and recovery behaviors of the printed specimen.
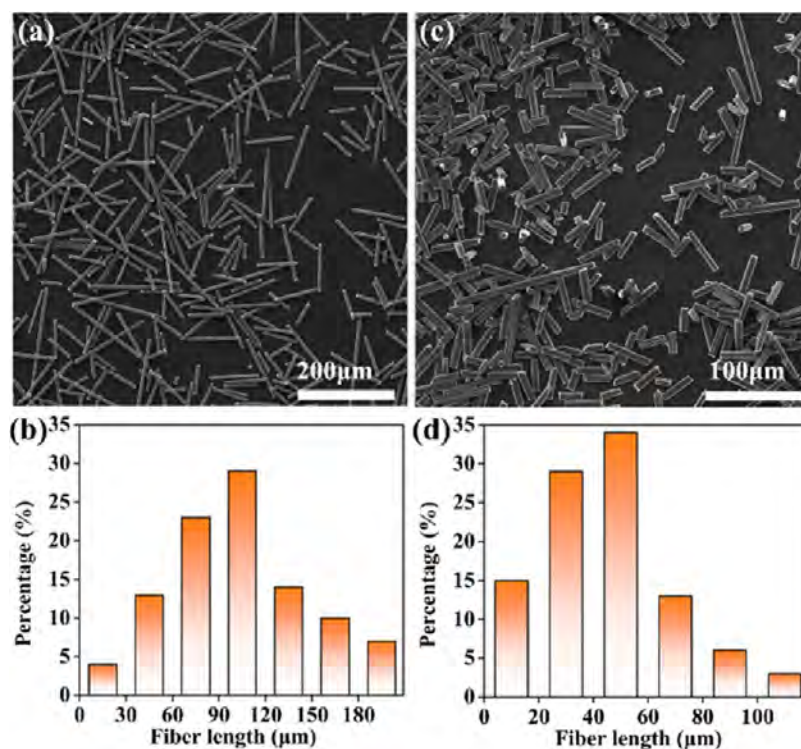
Figure 4. (a, b) SEM image of the CFs and the distribution diagram of the CF length and (c, d) SEM image of the GFs and the distribution diagram of the GF length.

The printed objects were manufactured by accumulating layers and the objects were anisotropic. The adhesion between layers affected the mechanical properties of printed objects. The CE30 ink had the highest printing accuracy among the three inks, so the CE30 ink was used to print the tensile samples. The tensile samples were printed in two different patterns. The layers were parallel to the axis of the tensile sample, as shown in Figure S7a, which was called the mode A

sample. The layers were perpendicular to the axis in Figure S7b called the mode B sample. The printed samples were UV post-cured and thermocured. The surface of the mode A sample was smooth, and that of the mode B sample was rough and pitted. The optical microscopy images clearly show the surface morphology of the two samples. An external force was applied to pull the sample apart. The stress−strain curves of the mode A and B samples are exhibited in Figure S8c, and the inserts are
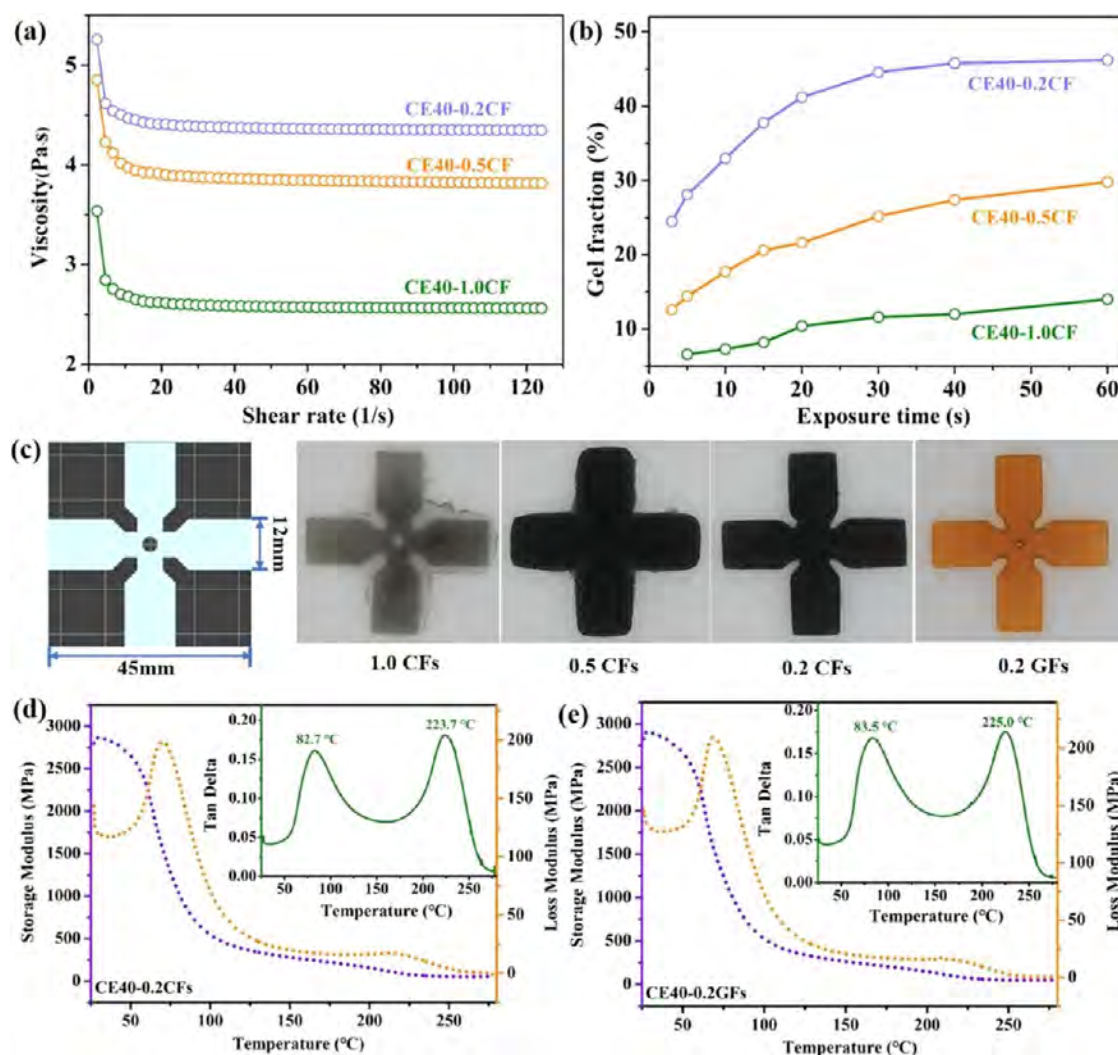
Figure 5. (a, b) Viscosity and F_w curves of different amounts of CF-doped CE40 inks; (c) windmill modeling and the profile display of 4D-printed windmills; and (d, e) DMA curves of 4D-printed CE40-0.2CF and CE40-0.2GF specimens.

fracture surface images of the samples. The fracture strain of the mode A sample is 17.1%, and the tensile strength is 53.6 MPa. The fracture surface is rough, and the cracks are radioactive. The fracture strain of the mode B sample is 7.7%, and the tensile strength is 31.9 MPa. The fracture surface is smooth, flat, and parallel to the print layer, demonstrating that brittle fracture occurs in the mode B sample. The reason is that defects between print layers lead to stress concentration. The fracture strain of the mode A sample is about 2.2 times that of the mode B sample. The main reason is that there are defects between print layers in the mode B sample, which lead to stress concentration.

The triple-shape memory cyanate composite can attract more attention to improve the application value of materials further. CFs and GFs were selected as fillers to enhance the thermal conductivity and mechanical properties of the CE resins. The SEM image and length distribution of the additive CFs and GFs are exhibited in Figure 4. The 60−120 μm long CFs account for 52%, and the 20−60 μm long GFs for 63%. The effects of CFs on the viscosity and F_w of the inks were studied. The viscosity curves show the shear-thinning behavior of different amounts of CF-doped CE40 inks, as shown in Figure 5a,b, which is caused by the orderly arrangement of

molecular chains under shear forces. The ink viscosity decreases with the increase in CF content because CFs make the molecular chain arrangement more orderly. The F_w increases gradually with exposure time. The addition of CFs greatly influences the photocuring of the inks. The F_w is 46.2% for CE40-0.2CFs and 14.0% for CE40-1.0CFs when the exposure time is 60 s.

The differences between the windmill modeling and the windmills printed with different inks are shown in Figure 5c. The CE40-1.0CF windmill print failed because of invalid adhesion produced between the print layer and the metal print platform, as shown in Figure S8. The layer exposure time (10 s) was not enough to cure a 50 μm layer of the CE40-1.0CF ink, forming a cross-linking gradient in the direction of layer thickness because CFs reflect and scatter UV lights. The side of the printing layer with a low cross-linking degree has less adhesion to the metal print platform leading to the failure of CE40-1.0CF and CE40-0.5CF windmills. The printed CE40-1.0CF and CE40-0.5CF windmills did not match the modeling, and the printed CE40-0.2CF and CE40-0.2GF windmills displayed a high matching degree with the modeling. The tan δ curves of the CE40-0.2CF and CE40-0.2GF specimens show two well-separated glass transition peaks because the fillers,
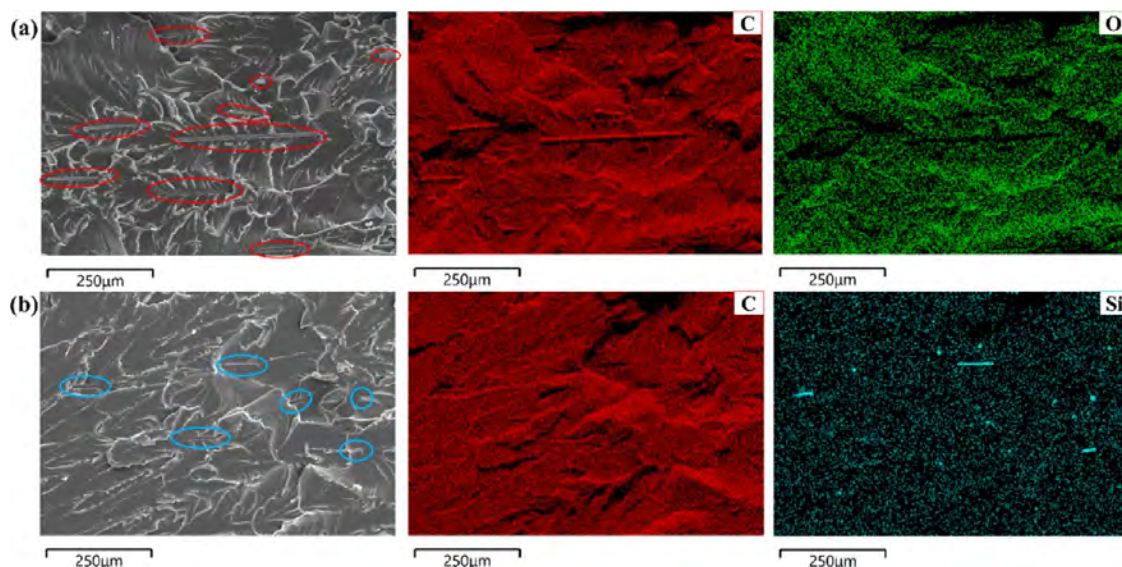
Figure 6. SEM-EDS maps of the fracture surfaces of (a) CE40-0.2CF specimen and (b) CE40-0.2GF specimen.
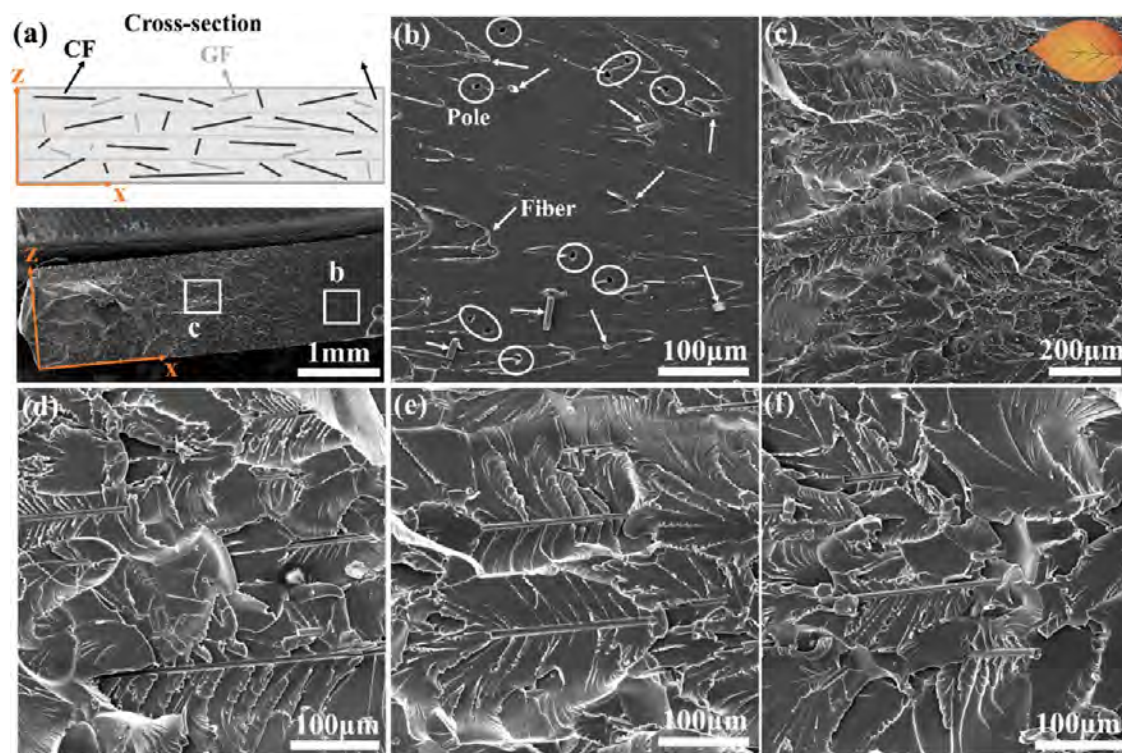
Figure 7. SEM images of the section of the 4D-printed tensile sample: (a) low-resolution image; (b) SEM image near the radiation center; (c) SEM image away from the radiation center; and (d−f) high-resolution images of GFs.

CFs and GFs, can facilitate phase separation.[7,39] The stress−strain curves in Figure S9 of the CE40-0.2CF and CE40-0.2GF specimens at room temperature reveal that the fracture strain of the CE40-0.2CF specimen increases by 21.6% and that of the CE40-0.2GF specimen increases by 10.8% compared to the PT-CE40 specimen.

The distribution of short CFs and GFs in CE40-0.2CFs and CE40-GFs was tested by SEM-EDS elemental mapping to study the effect of fillers on the properties of samples. The fracture surfaces of CE40-0.2CF and CE40-0.2GF samples are shown in Figure 6. The fibers can be clearly seen in the maps, and most of them are transversally distributed on the fracture

surface. For CE40-0.2CFs, many blank areas were found in the O map compared to the C map. The blank areas correspond to the CFs in the CE40-0.2CF resin. The distribution of CFs was not random in the resin. The printing layer is set to the *XY* plane during DLP printing. The fracture surface of the sample is perpendicular to the *XY* plane and set to the *XZ* plane, as shown in Figure 7. CFs are distributed in the *XY* plane inner layers due to the fact that each print layer thickness is 50 μm, and only CFs of length less than 50 μm can be randomly distributed in the print layer. More than 83% of the CFs were longer than 50 μm, and they tended to be arranged in the print layer. Therefore, the printed CF-reinforced composite
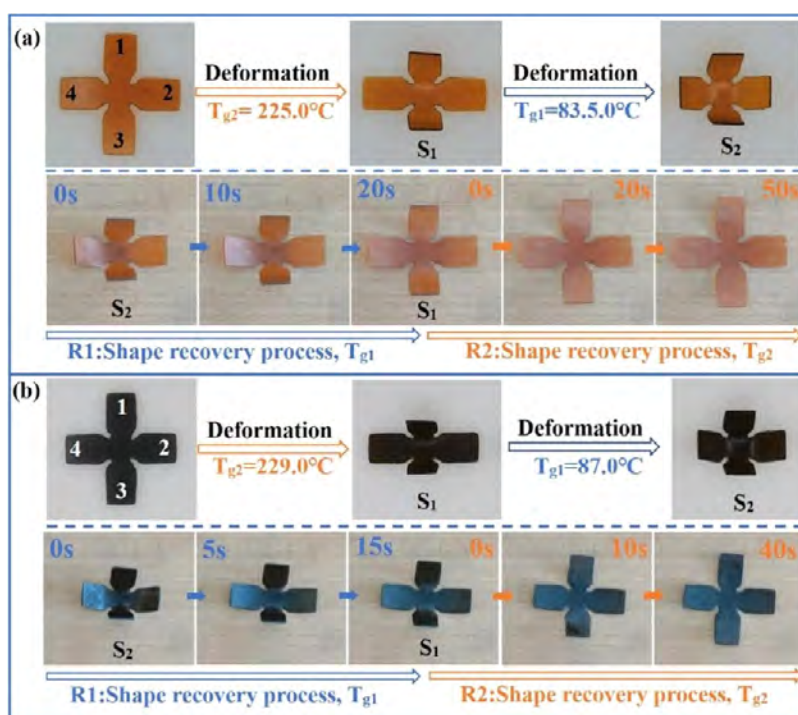
Figure 8. Triple-shape memory process of 4D-printed (a) CE40-0.2GF and (b) CE40-0.2GF-0.2CF windmills.
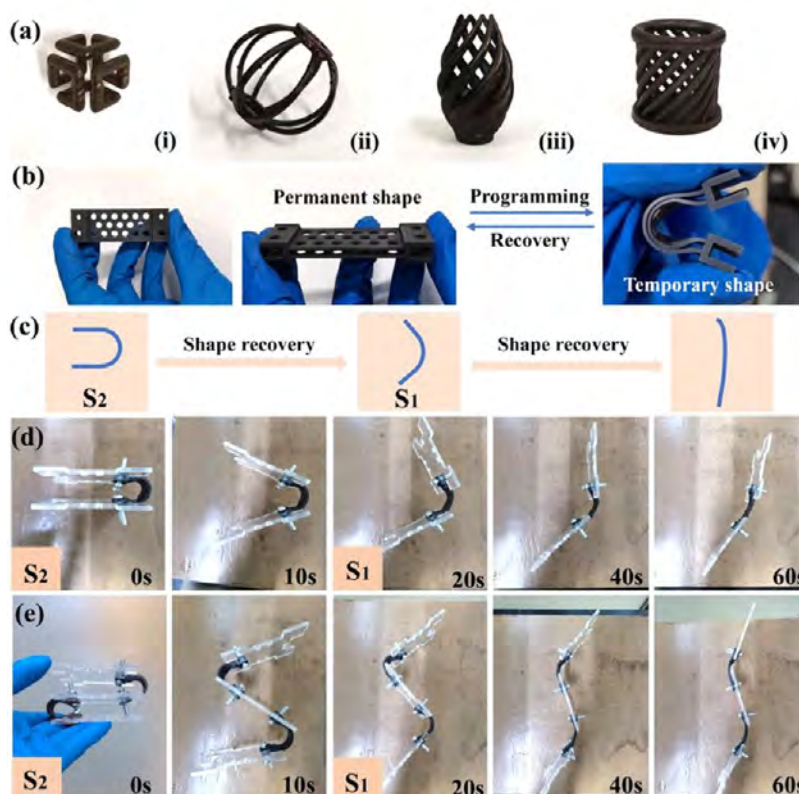
Figure 9. (a) Printed 3D structures; (b) printed double-layer hollow hinge; (c) shape recovery process of the temporary shapes (S_1 and S_2); and (d, e) deployment of the single-hinged-solar panel and double-hinged-solar panel.

structures are anisotropic. For CE40-GFs, the distribution patterns of C and O elements are basically consistent. There are many Si-intensive areas in the Si map; some are punctate, and some are fibrous, which correspond to the GFs in CE40-

GFs. Approximately 80% of the GFs in the resin are less than 60 μm in length, and most can achieve a random distribution in the print layer. Therefore, the GFs observed in the SEM image are shorter and have a random orientation.

0.2 wt% GFs and 0.2 wt% CFs were added into the CE40 resin to prepare the CE40-0.2GF-0.2CF composite, whose glass transition peaks and shape memory behavior are shown in Figure S10. The T_{g1} and T_{g2} are 87.0 °C and 229.0 °C, respectively. The specimen was heated to T_{g2} and then to T_{g1}, which was cooled to 25 °C again. The shape fixity ratio of the composite was calculated at 81.6%, and the shape recovery ratio is 80.0%, which is lower than that of the pure resin. The addition of fillers (GFs and CFs) decreases the shape memory performances of the resin, which is mainly due to the decrease of the cross-linking degree of the H- and L-networks. In Figure 7a, the schematic plot demonstrates the distribution characteristics of the CFs and GFs in the printing layers, and the section SEM image shows radial cracks. The SEM images with high magnification in Figure 7b−f are the sectional views of the tensile CE40-0.2GF-0.2CF sample. Brittle fractures mainly occurred near the radiation center, where the fibers were pulled out or broken. Ductile fractures mainly occurred in the region far from the radiation source. The cracks extended laterally from the fibers, and they were pinnate, which were similar to leaves with pinnate veins. The fibers stopped the cracks from spreading, which was why they toughened the sample.

The 4D-printed windmills were reshaped similarly to the flower. The 1st and 3rd blades were shaped into a temporary shape (S_1) at T_{g2}, and the 2nd and 4th blades were shaped in the other temporary shape (S_2) at T_{g1}. The shape recovery of the printed CE40-0.2GF windmill was compared to that of the printed CE40-0.2GF-0.2CF windmill, as shown in Figure 8. The shape recovery processes conducted at T_{g1} and T_{g2} were marked as R1 and R2, respectively. The difference between the two windmills is the recovery temperature in the process of shape recovery, which is 83.5 °C (T_{g1}) and 225.0 °C (T_{g2}) for the CE40-0.2GF windmill and 87.0 °C (T_{g1}) and 229.0 °C (T_{g2}) for the CE40-0.2GF-0.2CF windmill. The R_1 and R_2 are separate in the shape recovery process because of the composite with the well-separated glass transition peaks. The shape recovery time of the CE40-0.2GF-0.2CF windmill is shorter than that of the CE40-0.2GF windmill because of the good thermal conductivity of CFs.

In addition to the above two-dimensional (2D) structures, 3D structures, cubes, lanterns, stamens, and pen tubes (Figure 9a) could also be printed, indicating the good processing performance of the CE40-0.2GF-0.2CF composite ink. The prepared TSMCE has high fracture toughness, irradiation resistance, and triple-shape memory properties and can be used as an optimal material for space-deployable structures. The printed double-layer hollow hinge is shown in Figure 9b, which has the advantages of light weight, large deformation, and so on. The hinge can be shaped into a U-shape (S_2) and an L-shape (S_1); the shapes return to the original shape when the hinge is reheated. The two ends of the hinge are connected with two plastic plates, which simulate the solar panel. When the solar panel folds, the hinge is the temporary shape (S_2), and the hinge is heated to make the shape gradually recover, and the solar panel unfolds. Figure 9d,e shows the deployment of the single-hinged-solar panel and double-hinged-solar panel, which takes about 60 s. The deployment angle can be controlled due to the triple-shape memory performance of the printed hinge, which provides a new scheme for the multistage deployment function of solar panels.

4. CONCLUSIONS

A strategy was proposed for the IPN structure to prepare triple-shape memory polymers with high strength and fracture toughness via three-step curing, DLP 4D printing, UV post-curing, and thermal curing. The IPN structure endowed the polymer with two well-separated glass transition peaks (T_{g1} and T_{g2}) and triple-shape memory behaviors, improving the toughness and strength of the CE resins. Their storage modulus was more than 3.0 GPa, and the fracture strain was up to 10.9% at room temperature, illustrating better fracture toughness and strength of the printed TSMCE resins in comparison with the published data. In addition, the resins had good heat resistance. The incorporation of CFs and GFs facilitated the distinct separation of the two glass transition peaks benefiting distinguishing the two temporary shapes. The CFs and GFs significantly enhanced the toughness of the CE40 resin resulting in a 94% improvement in the fracture strain. Therefore, the prepared triple-shape memory CE resins and their composites have the characteristics of 4D printing, high strength, high fracture toughness, high-temperature resistance, and the advantages of adjustable material properties and large design freedom in applications. The strategy also provides necessary research strategies and perspectives for the in-depth study of dual-SMPs to multiple SMPs.

■ ASSOCIATED CONTENT

Ⓢ Supporting Information

The Supporting Information is available free of charge at https://pubs.acs.org/doi/10.1021/acsami.3c01750.

> CE monomer; the reactions in L-network and H-network; DMA curves of the P-CE40 specimen; TGA curves of CE30, CE40, and CE50 specimens; triple shape memory mechanism; failed and successful printing of the composite inks; stress−strain behaviors of GF- or CF-reinforced CE40 composites; DMA curves and shape memory loop curves of the CE40-0.2GF-0.2CF composite (PDF)

■ AUTHOR INFORMATION

Corresponding Author

Jinsong Leng − *Centre for Composite Materials and Structures, Harbin Institute of Technology (HIT), Harbin 150080, People's Republic of China;* ⓞ orcid.org/0000-0001-5098-9871; Email: lengjs@hit.edu.cn

Authors

Linlin Wang − *Centre for Composite Materials and Structures, Harbin Institute of Technology (HIT), Harbin 150080, People's Republic of China*

Fenghua Zhang − *Centre for Composite Materials and Structures, Harbin Institute of Technology (HIT), Harbin 150080, People's Republic of China*

Shanyi Du − *Centre for Composite Materials and Structures, Harbin Institute of Technology (HIT), Harbin 150080, People's Republic of China*

Complete contact information is available at:
https://pubs.acs.org/10.1021/acsami.3c01750

Notes

The authors declare no competing financial interest.

■ REFERENCES

(1) Peng, B.; Yang, Y.; Gu, K.; Amis, E. J.; Cavicchi, K. A. Digital Light Processing 3D Printing of Triple Shape Memory Polymer for Sequential Shape Shifting. *ACS Mater. Lett.* **2019**, *1*, 410−417.

(2) Bodaghi, M.; Damanpack, A. R.; Liao, W. H. Triple Shape Memory Polymers by 4D Printing. *Smart Mater. Struct.* **2018**, *27*, No. 065010.

(3) Behl, M.; Lendlein, A. Triple-shape Polymers. *J. Mater. Chem.* **2010**, *20*, 3335−3345.

(4) Li, J.; Xie, T. Significant Impact of Thermo-Mechanical Conditions on Polymer Triple-Shape Memory Effect. *Macromolecules* **2011**, *44*, 175−180.

(5) Narendra Kumar, U.; Kratz, K.; Behl, M.; Lendlein, A. Shape-Memory Properties of Magnetically Active Triple-Shape Nano-composites Based on a Grafted Polymer Network with Two Crystallizable Switching Segments. *Express Polym. Lett.* **2012**, *6*, 26−40.

(6) Du, J.; Liu, D.; Zhang, Z.; Yao, X.; Wan, D.; Pu, H.; Lu, Z. Dual-Responsive Triple-Shape Memory Polyolefin Elastomer/Stearic Acid Composite. *Polymer* **2017**, *126*, 206−210.

(7) Sabzi, M.; Ranjbar Mohammadi, M.; Zhang, Q.; Kargozar, S.; Leng, J.; Akhtari, T.; Abbasi, R. Designing Triple-Shape Memory Polymers from a Miscible Polymer Pair through Dual-Electrospinning Technique. *J. Appl. Polym. Sci.* **2019**, *136*, No. 47471.

(8) Behl, M.; Bellin, I.; Kelch, S.; Wagermaier, W.; Lendlein, A. One-Step Process for Creating Triple-Shape Capability of AB Polymer Networks. *Adv. Funct. Mater.* **2009**, *19*, 102−108.

(9) Zhang, Z.; Du, J.; Shan, W.; Ren, T.; Lu, Z. A Facile Approach toward Thermoplastic Triple-Shape Memory Polymers. *Macromol. Mater. Eng.* **2021**, *306*, No. 2000508.

(10) Yang, K.; Du, J.; Zhang, Z.; Ren, T. A Facile Strategy to Fabricate Robust Triple-Shape Memory Polymer. *Mater. Lett.* **2019**, *257*, No. 126753.

(11) Sivasankarapillai, G.; Li, H.; McDonald, A. G. Lignin-Based Triple Shape Memory Polymers. *Biomacromolecules* **2015**, *16*, 2735−2742.

(12) Song, Q.; Chen, H.; Zhou, S.; Zhao, K.; Wang, B.; Hu, P. Thermo- and pH-Sensitive Shape Memory Polyurethane containing Carboxyl Groups. *Polym. Chem.* **2016**, *7*, 1739−1746.

(13) Zhang, Q.; Wei, H.; Liu, Y.; Leng, J.; Du, S. Triple-Shape Memory Effects of Bismaleimide Based Thermosetting Polymer Networks Prepared via Heterogeneous Crosslinking Structures. *RSC Adv.* **2016**, *6*, 10233−10241.

(14) Wang, Y.; Pan, Y.; Zheng, Z.; Ding, X. Reconfigurable and Reprocessable Thermoset Shape Memory Polymer with Synergetic Triple Dynamic Covalent Bonds. *Macromol. Rapid Commun.* **2018**, *39*, No. 1800128.

(15) Rossegger, E.; Höller, R.; Reisinger, D.; Fleisch, M.; Strasser, J.; Wieser, V.; Griesser, T.; Schlögl, S. High Resolution Additive Manufacturing with Acrylate based Vitrimers using Organic Phosphates as Transesterification Catalyst. *Polymer* **2021**, *221*, No. 123631.

(16) Rossegger, E.; Höller, R.; Reisinger, D.; Strasser, J.; Fleisch, M.; Griesser, T.; Schlögl, S. Digital Light Processing 3D Printing with Thiol−Acrylate Vitrimers. *Polym. Chem.* **2021**, *12*, 639−644.

(17) Zhang, H.; Wang, D.; Wu, N.; Li, C.; Zhu, C.; Zhao, N.; Xu, J. Recyclable, Self-Healing, Thermadapt Triple-Shape Memory Polymers Based on Dual Dynamic Bonds. *ACS Appl. Mater. Interfaces* **2020**, *12*, 9833−9841.

(18) Wang, M.; Wang, L.; Xu, Y.; Fu, L.; Yang, H. One-Pot Fabrication of Triple Shape Memory Hydrogel Based on Coordination Bond, the Dynamic Borate Ester Bonds, and Hydrogen Bond. *Soft Matter.* **2019**, *17*, 342−349.

(19) Dai, L.; Song, J.; Qu, S.; Xiao, R. Triple-Shape Memory Effect in 3D-Printed Polymers. *Express Polym. Lett.* **2020**, *14*, 1116−1126.

(20) Du, H.; Liu, L.; Zhang, F.; Leng, J.; Liu, Y. Triple-Shape Memory Effect in a Styrene-Based Shape Memory Polymer: Characterization, Theory and Application. *Composites, Part B* **2019**, *173*, No. 106905.

(21) Xie, T.; Xiao, X.; Cheng, Y. Revealing Triple-Shape Memory Effect by Polymer Bilayers. *Macromol. Rapid Commun.* **2009**, *30*, 1823−1827.

(22) Podgórski, M.; Wang, C.; Bowman, C. N. Multiple Shape Memory Polymers Based on Laminates Formed from Thiol-Click Chemistry Based Polymerizations. *Soft Matter* **2015**, *11*, 6852−6858.

(23) Bae, C. Y.; Park, J. H.; Kim, E. Y.; Kang, Y. S.; Kim, B. K. Organic−Inorganic Nanocomposite Bilayers with Triple Shape Memory Effect. *J. Mater. Chem.* **2011**, *21*, 11288−11295.

(24) Tang, Z.; Gong, J.; Cao, P.; Tao, L.; Pei, X.; Wang, T.; Zhang, Y.; Wang, Q.; Zhang, J. 3D Printing of a Versatile Applicability Shape Memory Polymer with High Strength and High Transition Temperature. *Chem. Eng. J.* **2022**, *431*, No. 134211.

(25) Li, Z.; Hu, J.; Ma, L.; Liu, H. High Glass Transition Temperature Shape-Memory Materials: Hydroxyl-Terminated Poly-dimethylsiloxane-Modified Cyanate Ester. *J. Appl. Polym. Sci.* **2020**, *137*, No. 48641.

(26) Li, Z.; Hu, J.; Ma, L.; Liu, H. Shape Memory CTBN/Epoxy Resin/Cyanate Ester Ternary Resin and Their Carbon Fiber Reinforced Composites. *J. Appl. Polym. Sci.* **2020**, *137*, No. 48756.

(27) Wang, L.; Zhang, F.; Liu, Y.; et al. Thermal, Mechanical and Shape Fixity Behaviors of Shape Memory Cyanate under γ-ray Radiation. *Smart Mater. Struct.* **2022**, *31*, 45010.

(28) Wang, L.; Zhang, F.; Liu, Y.; et al. γ-rays Radiation Resistant Shape Memory Cyanate Ester Resin and Its Composites with High Transition Temperature. *Smart Mater. Struct.* **2019**, *28*, 75039.

(29) Xie, F.; Liu, L.; Gong, X.; Huang, L.; Leng, J.; Liu, Y. Effects of Accelerated Aging on Thermal, Mechanical and Shape Memory Properties of Cyanate-Based Shape Memory Polymer: I Vacuum Ultraviolet Radiation. *Polym. Degrad. Stabil.* **2017**, *138*, 91−97.

(30) Xie, F.; Huang, L.; Liu, Y.; Leng, J. Synthesis and Characterization of High Temperature Cyanate-Based Shape Memory Polymers with Functional Polybutadiene/Acrylonitrile. *Polymer* **2014**, *55*, 5873−5879.

(31) Xie, F.; Gong, X.; Huang, L.; Liu, L.; Leng, J.; Liu, Y. Effects of Accelerated Aging on Thermal, Mechanical, and Shape Memory Properties of a Cyanate-Based Shape Memory Polymer: II Atomic Oxygen. *Polym. Degrad. Stabil.* **2021**, *186*, No. 109515.

(32) Hatta, M.; Shinya, A.; Gomi, H.; Vallittu, P. K.; Säilynoja, E.; Lassila, L. V. J. Effect of Interpenetrating Polymer Network (IPN) Thermoplastic Resin on Flexural Strength of Fibre-Reinforced Composite and the Penetration of Bonding Resin into Semi-IPN FRC Post. *Polymers* **2021**, *13*, 3200.

(33) Takado, K.; Ube, T.; Ikeda, T. Photomobile Polymer Materials with Double Network Structures: Crosslinked Azobenzene Liquid-Crystalline Polymer/Methacrylate Composites. *Mol. Cryst. Liq. Cryst.* **2014**, *601*, 43−48.

(34) Zhang, L.; Jiao, H.; Jiu, H.; Chang, J.; Zhang, S.; Zhao, Y. Thermal, Mechanical and Electrical Properties of Polyurethane/(3-aminopropyl) Triethoxysilane Functionalized Graphene/Epoxy Resin Interpenetrating Shape Memory Polymer Composites. *Composites, Part A* **2016**, *90*, 286−295.

(35) Vallittu, P. K. Interpenetrating Polymer Networks (IPNs) in Dental Polymers and Composites. *J. Adhes. Sci. Technol.* **2009**, *23*, 961−972.

(36) Chandrasekaran, S.; Duoss, E. B.; Worsley, M. A.; Lewicki, J. P. 3D Printing of High Performance Cyanate Ester Thermoset Polymers. *J. Mater. Chem. A* **2018**, *6*, 853−858.

(37) Zhou, Z.-X.; Li, Y.; Zhong, J.; Luo, Z.; Gong, C.; Zheng, Y.; Peng, S.; Yu, L.; Wu, L.; Xu, Y. High-Performance Cyanate Ester Resins with Interpenetration Networks for 3D Printing. *ACS Appl. Mater. Interfaces* **2020**, *12*, 38682−38689.

(38) Wang, L.; Zhang, F.; Liu, Y.; Du, S.; Leng, J. Photosensitive Composite Inks for Digital Light Processing Four-Dimensional Printing of Shape Memory Capture Devices. *ACS Appl. Mater. Interfaces* **2021**, *13*, 18110−18119.

(39) Sabzi, M.; Babaahmadi, M.; Rahnama, M. Thermally and Electrically Triggered Triple-Shape Memory Behavior of Poly(vinyl acetate)/Poly(lactic acid) Due to Graphene-Induced Phase Separation. *ACS Appl. Mater. Interfaces* **2017**, *9*, 24061−24070.